Aeroacoustic Performances of the ECL5 UHBR Turbofan Model With Serrated OGVs: Design, Predictions and Comparisons With Measurements

Martin Buszyk, Cyril Polacsek, Thomas Le Garrec, Raphaël Barrier, Edouard Salze, Jacky Marjono

Aeroacoustic performances of the ECL5 UHBR turbofan model with serrated OGVs: design, predictions and comparisons with measurements

M. Buszyk[1], C. Polacsek[2] and T. Le Garrec[3]
DAAA, ONERA, Institut Polytechnique de Paris, 92320, Châtillon, France

R. Barrier[4]
DAAA, ONERA, Institut Polytechnique de Paris, 92190, Meudon, France

E. Salze[5]
Ecole Centrale de Lyon, LMFA, 69130 Ecully, France

J. Mardjono[6]
YXAR – Safran Aircraft Engines, Moissy-Cramayel, 77550, France

This work is devoted to the design and evaluation of a low-noise OGV aiming to reduce the rotor-stator interaction noise using leading edge serrations and tested on the ECL5 UHBR model in the PHARE-B3 rig at Ecole Centrale Lyon. First, a radially varying 2D design is proposed and evaluated by means of a fast analytical prediction tool and using a strip approach. Then, an iterative process combining 3D RANS calculations with an in-house modeler is carried out to achieve a suitable 3D geometry, while minimizing the aerodynamic penalties. Following this design process, high fidelity simulations based on a lattice-Boltzmann solver are performed to assess the sound power level reduction achieved by the serrated OGV (by comparison to the untreated baseline case primarily tested). Due to the low-compressibility assumptions of the present LBM, simulations are limited to the reachable higher regime (45% of nominal rotational speed). Hence, available analytical and numerical predictions are compared to the experimental data, both in terms of aerodynamic and acoustic performances. A rather good agreement is obtained with sound power level reductions up to 3 dB from intake radiation and 6 dB in the bypass duct on the considered operating points.

Nomenclature

ADP = *Aerodynamic Design Point*
APP = *Approach*
CAA = *Computational AeroAcoustics*
LE = *Leading Edge*
LES = *Large Eddy Simulation*
FWH = *Ffowcs-Williams and Hawkings*

[1] Research Engineer, Aerodynamics Aeroelasticity Aeroacoustics Department, martin.buszyk@ONERA.fr
[2] Senior Research Engineer, Aerodynamics Aeroelasticity Aeroacoustics Department, cyril.polacsek@ONERA.fr
[3] Research Engineer, Aerodynamics Aeroelasticity Aeroacoustics Department, thomas.le_garrec@ONERA.fr
[4] Research Engineer, Aerodynamics Aeroelasticity Aeroacoustics Department, raphael.barrier@ONERA.fr
[5] Research Engineer, UMR 5509, edouard.salze@ec-lyon.fr
[6] Expert of Aerodynamics & Acoustics Department at Safran Aircraft Engines, jacky.mardjono@safrangroup.com

LBM = *Lattice Boltzmann Method*
OAPWL = *OverAll PoWer Level (dB)*
OGV(s) = *Outlet Guide Vane(s)*
OP(s) = *Operating Point(s)*
PSD = *Power Spectrum Density (dB/Hz)*
PWL = *PoWer Level (dB or dB/Hz)*
RANS = *Reynolds Averaged Navier Stokes*
RMS = *Root Mean Square*
RPM = *Revolutions Per Minute*
RSI = *Rotor Stator Interaction*
SPL = *Sound Pressure Level (dB)*
TI = *Turbulence Intensity (%)*
TLS = *Turbulence Length Scale (longitudinal integral length scale) (m)*
UHBR = *Ultra High Bypass Ratio*
WH = *Wiener-Hopf*
WMLES = *Wall Modeled Large Eddy Simulation*

I. Context and objectives

Although engine manufacturers are pushing towards disruptive architectures such as the open fan, UHBR turbofan is still remaining the most conventional short-term solution. For both cases, increasing technology readiness level concepts, priory based on passive treatments, are highly required to reach the ACARE targets in terms of EPNL (Effective Perceived Noise Level) reduction. In this context, ONERA is designing low-noise OGVs characterized by leading edge serrations in close collaboration with SAE (Safran Aircraft Engines) [1]. A new test bench, named PHARE-B3, has been also recently implemented at ECL in order to perform aerodynamic and acoustic test campaigns on realistic UHBR fan modules [2][3][4]. In particular, this test facility allows to experimentally investigate noise reduction technologies in industrial configurations.

In the present work, the focus is put on designing and evaluating silent stator stages in view of reducing the RSI noise which is expected to be the major contributor to the overall aeroengine broadband noise. Although passive treatments based on wavy leading edges have been widely studied for the mitigation of turbulence airfoil interaction noise, most of these works were restricted to simplified configurations [3][32]. From the authors knowledge, this study constitutes the first numerical and experimental comparison of noise reduction enabled by serrations on a realistic turbofan model, although a few recent numerical simulations have assessed the implementation of wavy leading edges on fan-OGV stages. Studies encompassing both aerodynamic control (by RANS) and acoustic performances (by CAA) have been carried out in [1]. A LES simulation of a single stage axial fan with LE serrations has been recently investigated by Tong [33] with a reduction of the broadband noise up to 4 dB. 360° simulations more easily tackled by LBM were also conducted with to wavy LE. In [34], serrations and porous serrations for stator vanes have been respectively considered on the up-scaled NASA-SDT turbofan mounted on the HL-CRM. Although a rather small broadband noise reduction has been achieved, this study outlines what could be the future of aeroacoustic simulations for a comprehensive evaluation of noise reduction technologies as close as possible to performances achieved during certification conditions. Although serration have been assessed in terms of pressure and drag coefficients up to the impact on engine thrust, very few works as those conducted by ONERA have quantified the impact of such treatments on aerodynamic penalties and implemented strategies for designing 3D shapes starting from 2D acoustic-purpose serration patterns in order to reduce those penalties [1][7][8]. Implementing serrations on future aeroengines is both an aerodynamical and an aeroacoustical challenge, which implies that the extension of serrated airfoils from academic configurations to fan-OGV applications is quite unusual and an open-ended topic. This is particularly true given that the accurate characterization of the turbulent flow in the fan-OGV interstage remains a crucial point [23] for aeroacoustics, considering that analytical models and design rules proposed in the literature mostly focus on simplified turbulence assumptions, except some attempts to include anisotropy effects [26].

Regarding the prediction methods, sound reduction from leading edge serrations can be estimated by means of recent analytical formulations based on the Wiener-Hopf technique [8], but high-fidelity predictions on relevant

configurations (with almost no approximations) can be fully assessed using LBM simulations [10][11]. Both approaches are considered in the present study to evaluate ONERA's low-noise design applied to the ECL5 fan-OGV stage.

The paper is structured as follows. After a short presentation of the ECL5 turbofan model in section II, the section III discusses the serrated OGV design, covering basic 2D acoustic design, with raw estimation of acoustic performances, 3D design extension with control of aerodynamic penalties, and manufacturing of selected geometry (performed by COMOTI). Then main section IV is devoted to the LBM simulations limited to a low-speed regime (45 Nn), describing the numerical setup, and discussing aerodynamic results and acoustic predictions. Finally, the comparisons with PHARE measurements are presented in section V.

II. ECL5 turbofan model presentation

The UHBR engine considered for this study is the ECL5 turbofan model shown in Fig. 1 [4]. The nacelle diameter is roughly equal to 0.25 meter and the engine is composed of 16 fan blades and 31 outlet guide vanes (OGV). The revolution speed at nominal regime (100 Nn, denoted ADP) is equal to 11000 RPM and the approach condition is at 55 Nn (6050 RPM) and denoted APP. All operating conditions discussed here are defined at the design point working line. This turbofan model (baseline case) has been tested in the PHARE ECL-B3 test facility (see Fig. 2) by mid 2023 and the low-noise serrated OGV designed by ONERA has been tested recently in January 2024.

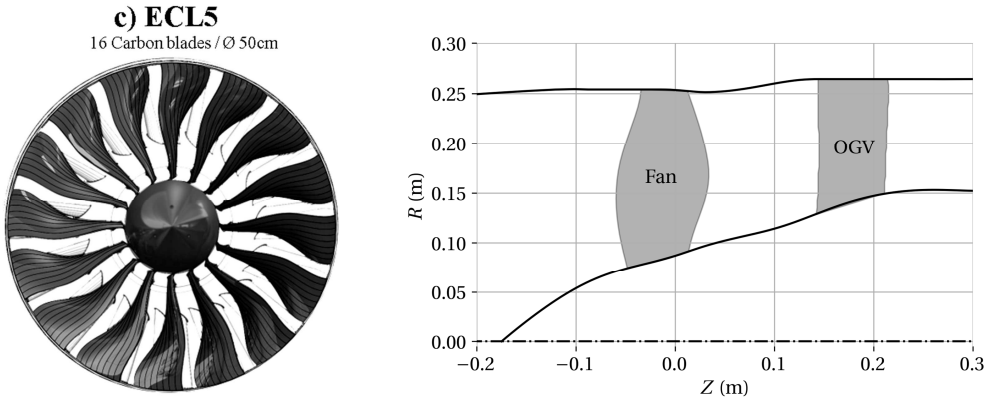

Fig. 1 ECL5 fan front view (left) and fan-OGV stage meridian geometry (right) [4].

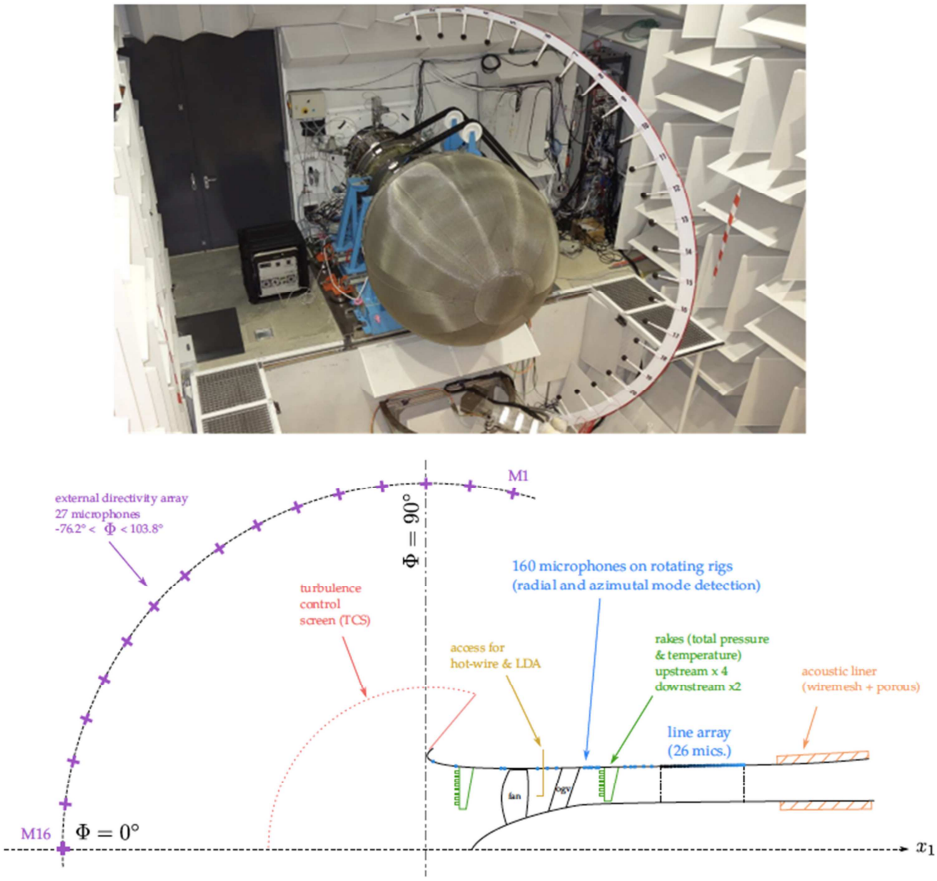

Fig. 2 Picture of PHARE ECL-B3 test facility (top) and sketch of the rig with main instrumentation (bottom), from [20].

The picture in Fig. 2 clearly shows the turbulence control screen surrounding the intake and the external microphone circular antenna. A total of 187 microphones are used in the test-rig to provide extensive data of the noise radiation of the rotor-stator stage. These microphones are distributed as follows: (1) a total of 27 microphones upstream of the duct, mounted on a 2 meters radius circle that can be rotated around the vertical axis so as to represent the directivity on a portion of a sphere, and (2) 160 randomly-distributed microphones, some of whom are mounted on rotating rigs, are used to extract the modal amplitudes of the pressure in the duct. More details and analyzes of these tests are discussed in a complementary ECL paper [20].

III. Serrated OGV design

A. 2D acoustic design using inflow turbulence characteristics

Starting form ECL-5 baseline geometry, a 2D LE serration design based on sinusoidal patterns has been derived from simple rules and using turbulence length scale characteristics provided by CFD calculations (previously performed by ECL [21]). The parametric laws adopted to draw the serrations are those proposed by Polacsek [1]:

- $\lambda_s \approx 2$ TLS
- $h_s/\lambda_s \approx 1$

where λ_s and h_s are respectively the serration wavelength and serration amplitude, and TLS is the estimated (longitudinal) integral length scale of the turbulent flow impacting the vane in the LE region. This scale was prescribed at 55 Nn (approach condition) by considering the radial profile issued from a WMLES solution (Fig. 3), extracted closely upstream to the LE position. As discussed in [1], a strip approach (Fig. 4, left) is used to match the radial profile and to set the suitable strip values for λ_s and h_s, leading to the initial 2D design shown in Fig. 4, right.

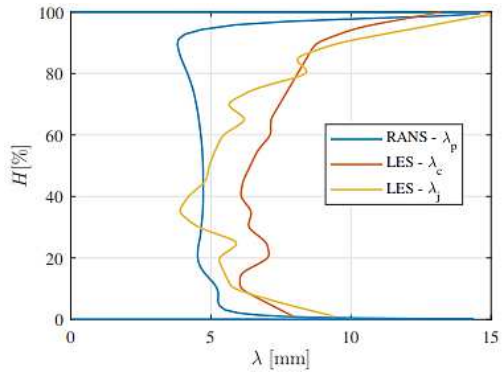

Fig. 3 TLS profiles over the span assessed from CFD at 55 Nn: ONERA design based on λ_c profile (orange curve) from WMLES solution [21].

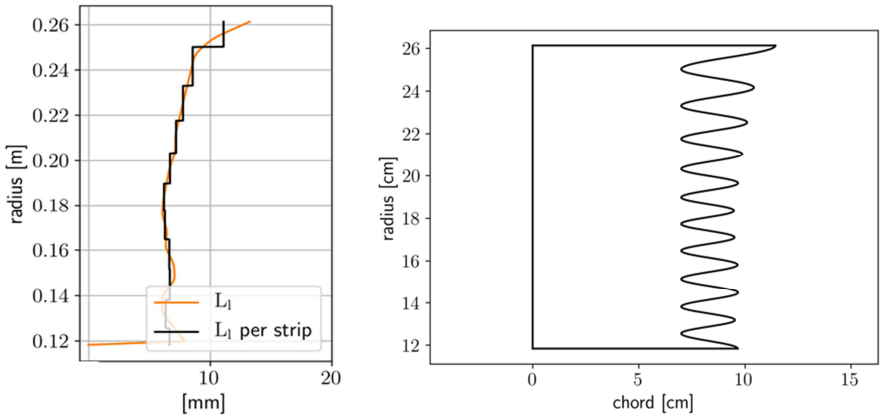

Fig. 4 Strip approach for setting the evolutive patterns (left) and 2D flat-plate design (right).

B. Acoustic performances at design stage

A raw estimation of acoustic performances (in the design step) has been first performed using a fast prediction tool (*MATLAB* code) based on the Wiener-Hopf formulation proposed by Ayton [8]. This model is valid for a flat-plate with infinite chord and span, but geometrical corrections for practical application to actual span length (without need of recalibration) have been proposed by Buszyk and validated in Ref. [1]. Furthermore, in order to take into account the radial evolution of the serration patterns, a strip approach is introduced for the evaluation process (solving the problem for each strip and performing a non-coherent sum). A few assessments of sound power level reduction (ΔPWL spectra) are plotted in Fig. 5 at APP (ECL WMLES-based inputs) and ADP (ONERA RANS-based inputs) conditions. Estimations issued from the empirical "log law" evidenced by Paruchuri [3] (academic open-jet rig experiments with isolated airfoils mounted beyond a turbulence grid), are also plotted for comparison. Significant PWL reductions (reaching 6.5 dB at APP) are clearly highlighted with a reasonable agreement with the "log law", despite more important deviations at ADP. An OAPWL reduction of at least 4 dB, obtained by integrating the levels in the frequency range [0.5 BPF - 3 BPF], is expected for both OPs, which is quite promising.

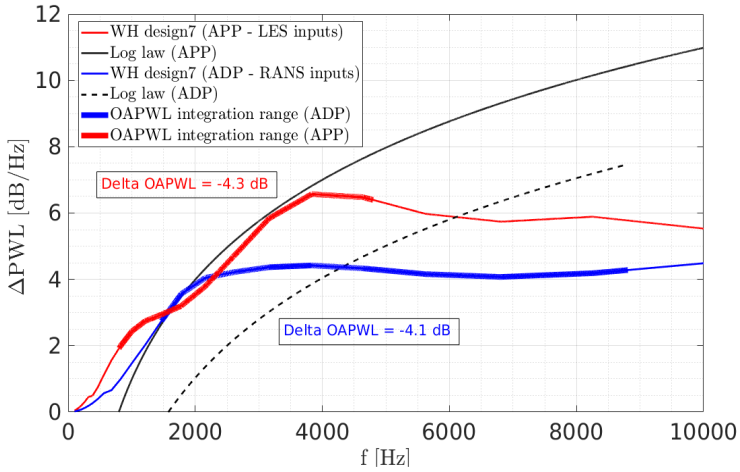

Fig. 5 ΔPWL spectra issued from WH model and empirical log law at APP and ADP.

C. 3D aerodynamic design using RANS to reach acceptable penalty targets

Starting from the initial 2D design, a 3D extension is then realized using an in-house modeler (*ersatZ*) and by performing iterative RANS calculations (with *elsA* ONERA code). The focus is put on ADP, in order to reach the targets specified by SAE in terms of aerodynamic penalties and final integration purpose. Several local modifications have been proposed from the initial design (design V1) to the last manufactured design (design V7) plotted in Fig. 6. This low-noise design so obtained is expected to ensure acceptable aerodynamic penalties as demonstrated in Fig. 7, both in terms of isentropic efficiency (-0.4 point penalty) and pressure loss coefficient (-0.12 point penalty).

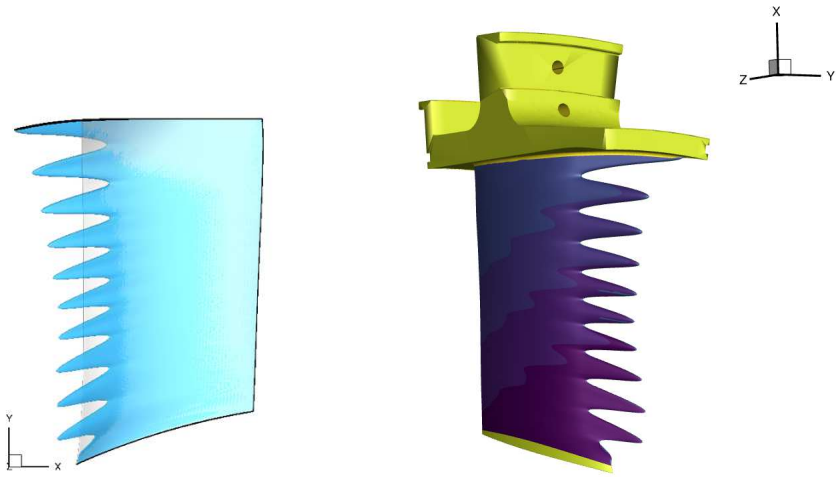

Fig. 6 Low-noise ONERA serrated OGV (last design V7, left) and CAD view including the attachments (right).

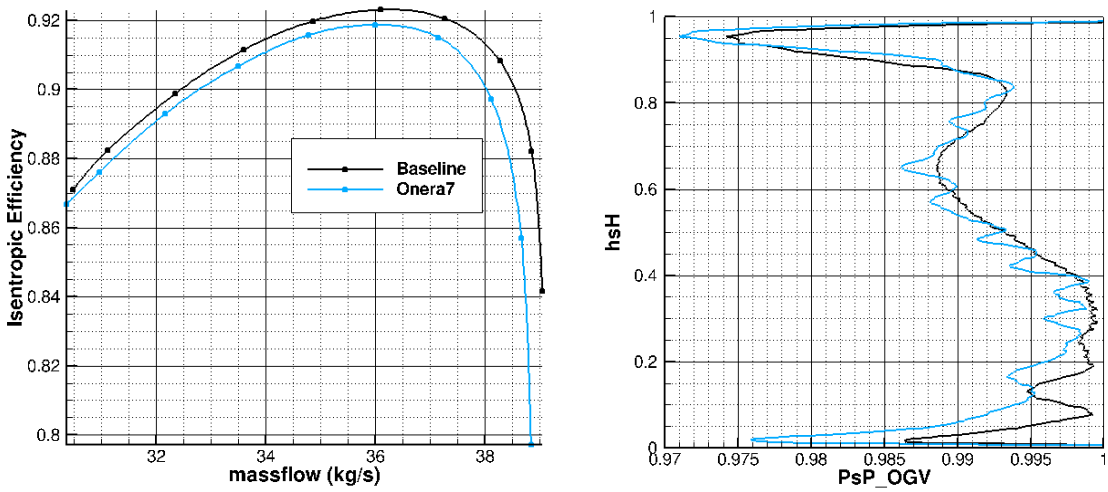

Fig. 7 Aerodynamic penalties in terms of isentropic efficiency (left) and pressure loss coeff. (right).

D. OGVs manufacturing (by COMOTI)

After specific computations carried out by COMOTI to check the mechanical behavior (not discussed here), the serrated blades have been manufactured (by COMOTI too) using CNC machining. Photography of the end product (totalizing 31 vanes) is shown in Fig. 8.

Fig. 8 Manufactured serrated vanes.

IV. LBM simulations at 45 Nn

A. Overview of the main *ProLB v2.8* features

The LBM simulations have been performed with the code *ProLB* [12] using available functionalities. The key features are the following. In contrast with traditional CFD solvers relying on the Navier-Stokes (NS) equations, in the LBM, the fluid is described by probability distribution functions describing the fluid particles. In the present case the discretization is performed on a D3Q19 lattice distribution function. For quasi-incompressible flows, this discrete formulation involving nineteen velocities allows the computation of the athermal formulation of the NS equations [13]. On this D3Q19 lattice, which is in other words the octree mesh of the simulation, the evolution of the distribution function can be governed by a two-step algorithm often called "stream and collide". Collisions take place locally and the streaming operation is performed following the octree lattice while staying exact thanks to the Courant-Friedrichs-Lewy (CFL) equal to 1. This makes this step non-dissipative and its numerical implementation quite simple and cost effective since coarser mesh cells have a smaller time step. The CPU efficiency and very low numerical dissipation make the solver suitable for aeroacoustic simulations. Additionally, immersed boundary

conditions handle geometries, around which the fluid boundary layer is resolved thanks to an advanced wall log-law taking into account an adverse pressure gradient and curvature effects [14][15]. In the present work, LBM simulations are carried out with the *ProLB* solver in the 2.8 version. In *ProLB,* an advanced collision operator, the hybrid recursive regularized (HRR) operator is implemented, enhancing the stability of the scheme and reducing the spurious noise at mesh refinement transition along with high order correction terms to remove $O(M^3)$ errors [16], leading to a more robust code below M=0.7 [17]. As for turbulence modeling, in *ProLB*, the Shear-Improved Smagorinsky Model (SISM) [18] is employed as a subgrid-scale viscosity to model unresolved eddies, similarly to traditional CFD solvers Finally, to reduce spurious noise source generation at mesh transitions due to the advection of the variables across grid refinements, the Direct Coupling (DC) cell-vertex algorithm is used [19].

Since the actual version of *ProLB* available at ONERA is the low-compressible one, practical limitations for current applications are trimmed by the local flow Mach number values that should be locally lower than 0.7. This constraint is affecting the set-up of the LBM simulation. For this reason, the higher reachable regime for the present configuration was 45 Nn (4950 rpm), with a targeted OP condition roughly corresponding to the blue circle on the working line of the fan map characteristics (initially starting from 50 Nn) shown in Fig. 9 with a total pressure ratio and a mass flow rate respectively around 1.05 to 1.06 and 18 to 19 kg/s. Even though, this off-chart regime had to be considered, several chained calculations had been needed with an increasingly fine mesh to avoid over-speeds during the transitional period, as illustrated during aerodynamic analysis in III.B.

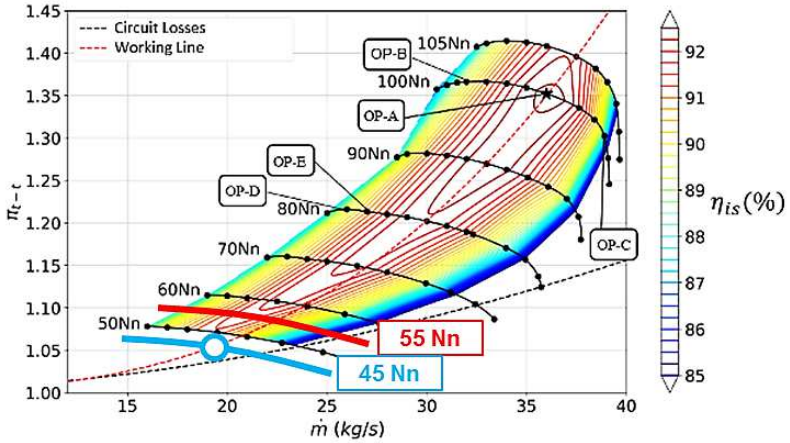

Fig. 9 ECL5 fan map characteristics [4][5].

Concerning the geometrical elements which have been simulated, the full engine rig is included in the LBM numerical set-up (Fig. 10), without taking into account the TCS (Turbulence Control Screen) and the volute system of course. Three-dimensional views of the hub and shroud surfaces with the fan-OGV rows are presented in Fig. 11, left and right, respectively for the baseline and low-noise serrated OGV. No valve control law being available in this version of *ProLB* used here, it has been decided to extend with a slip condition the duct downstream making the flow free to leave out from the outlet open section. The external fluid is set at rest with standard atmospheric static pressure. A rigid conical exhaust with a slip wall condition, which can be seen in Fig. 10, is added to avoid the sound waves radiation towards the upstream direction (which could pollute the acoustic field generated from the intake). It has been checked that such a cone has a negligible effect on the aerodynamic behavior. However, the absence of a winnowing law with radial equilibrium implies that the operating point will naturally be set. This does not pose any major problems for airflow and aerodynamic comparisons, either with experimental data or RANS simulations, as several winnowing points are scanned in these cases, the closest one being chose for cross comparisons performed here. Finally, it has to be highlighted that all simulations presented here have been carried out prior to the test campaign.

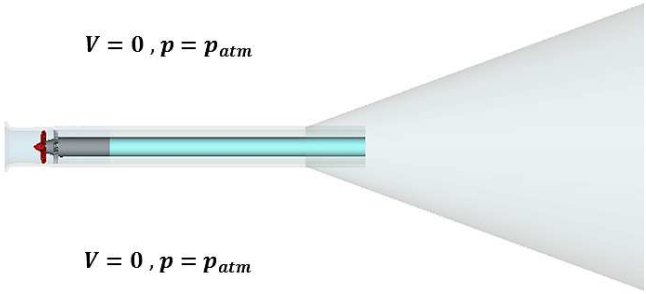

Fig. 10 LBM set-up for PHARE-B3 rig simulations.

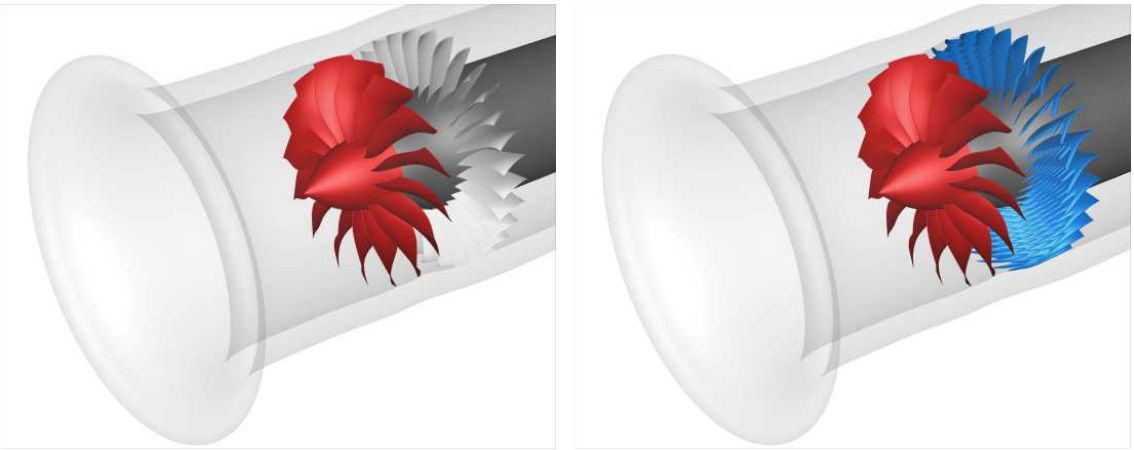

Fig. 11 3D views of skin mesh of hub and shroud with the fan-OGV rows: baseline OGV (left) and low-noise serrated OGV (right).

The octree mesh consists of several refinement levels with a doubling of the mesh size at each transition. All solid boundaries in the Fan-OGV stages (stator, rotor, hub, and shroud) are protected at least 6 layers of approximately 0.2 mm mesh size. The finest level is however located in the tip region (with 0.1 mm) in order to ensure at least 7 points. The choice of meshing the tip region has been motivated from RANS computations performed at 55 Nn (and a mass flow rate of 21 kg/s) with the rotor alone. In the shroud region, a more intense production of turbulent kinetic energy is visible if the tip gap is modeled (Fig. 12, top left) in contrast to the case where the blades are extended to the shroud (Fig. 12, bottom left). This is highlighted in the plane corresponding to OGV leading edge (in the full set-up configuration) in Fig. 12, right, revealing the radial evolution of the turbulence intensity. This figure also illustrates the fact that the hub and shroud regions should be major contributors to the RSI noise sources and of from a more general perspective of prime importance during the design of silent OGVs.

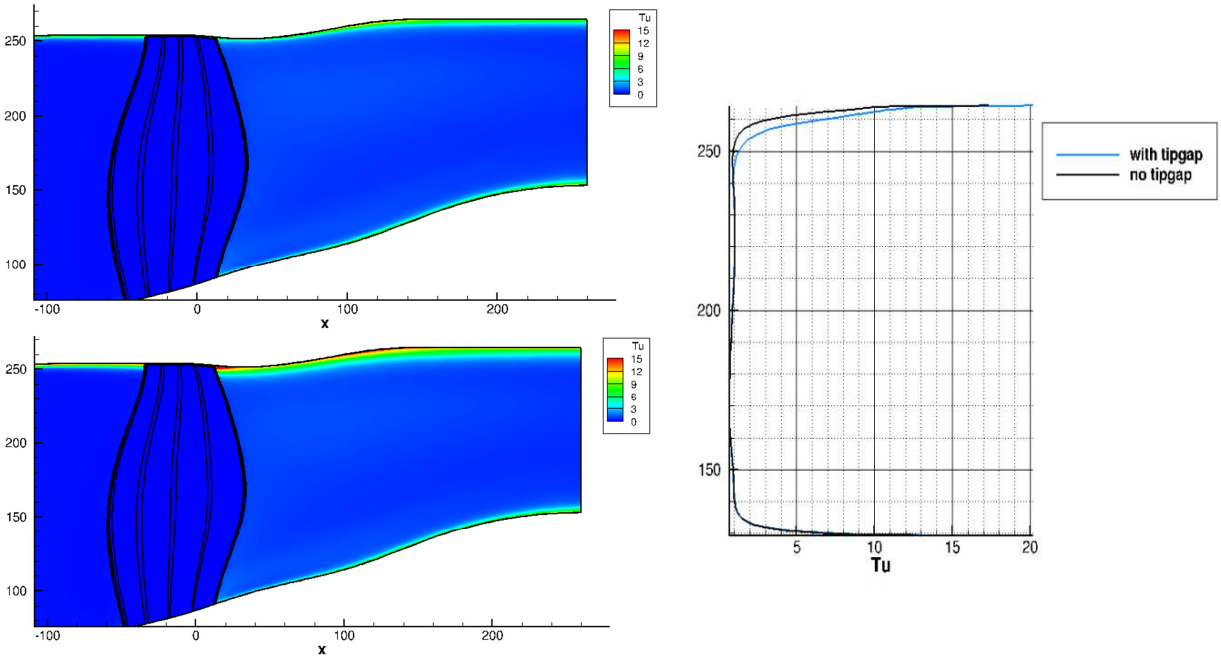

Fig. 12 Cut views of the turbulent intensity from a rotor alone RANS simulation at 55 Nn: blade extended up to the shroud (top) and taking into account the tip gap (Bottom). Radial evolution of the circumferentially averaged turbulence intensity (right).

The octree mesh near the rotor tip is displayed in Fig. 13 (left). The inter-stage turbulence propagates in the fourth resolution layer with cells of approximately 0.9 mm size. Several successive refinement jumps are then considered up to the far-field boundary conditions set at rest and protected by sponge's zones to dissipate residual waves at low frequencies and avoid parasitic reflections. In order to limit the memory footprint linked to the total number of points, two half-spheres are considered at 1 and 2 m radius from the inlet plane, for the propagation of the downstream acoustic waves, with approximate cut-off frequencies equal to 6 and 12 kHz with 8 points per wavelength.

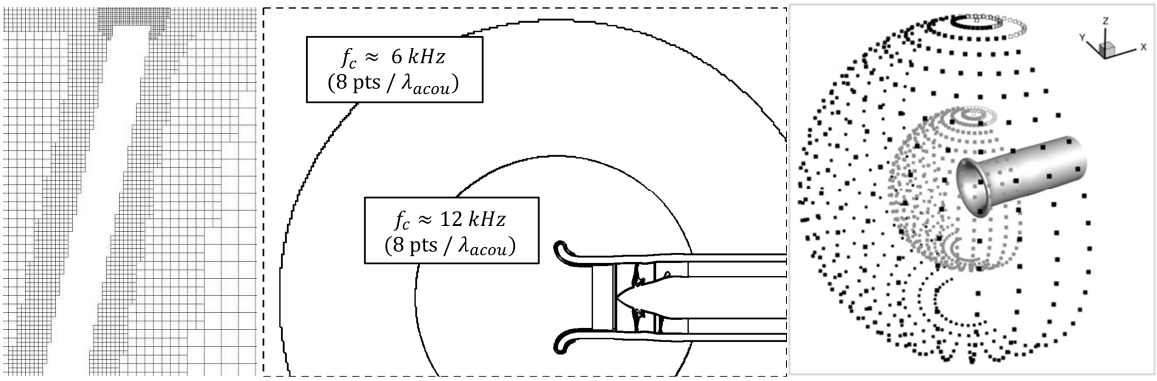

Fig. 13 Zoom on the mesh (fine case) around tip gap (left). Mesh transitions in the intake region (middle). Intake region with specific extraction probes over half-spheres for radiated sound field analyzes (right).

Closer views around the intake region are displayed in Fig. 13 (middle), are revealing two half-spheres, the larger sphere matching the position of the microphone antenna (visible on PHARE-B3 facility in Fig. 2). In addition to the experimental far-field microphone array which is reproduced in the numerical domain, a second sphere with half

diameter has been also added in order to provide acoustic data taking advantage of the finer mesh up to 1m from the inlet as illustrated in Fig. 13. Among several outputs (volume fields, surface extraction and point probes), turbulent wall pressure on blades and vanes are stored in order to feed a FWH-based in-house code (*FanNoise*), solving the loading noise generated and propagated in the duct (with annular geometry and uniform mean flow assumptions). These LBM+FWH predictions allow in particular assessing the contribution of OGV sources expected to be attributed to the RSI mechanism and separate them from rotor alone sources.

Finally, regarding HPC performances, the fine mesh designed for acoustic predictions totalizes about 1 billion points and the simulations are performed over 3600 cores with a simulation time covering 12 revolutions, corresponding to a duration of 0.12 s. The required CPU time is equal to 410 khours leading to a restitution time around 3.6 days on ONERA's NEC SATOR supercomputer.

B. Steady and unsteady aerodynamic analyzes

Several consecutive computations have been launched using different sets of grids (adjusting the refinement levels) to reach the target mass flow rate by adopting a multi-field mapping strategy. This is illustrated in Fig. 14, left, showing the progressive convergence of the mass flow rate, using successive coarse/medium/fine grids, to the expected value of 18.5 kg/s (issued from a RANS calculation performed with *elsA* code). The average variables appear to converge after a transient lasting about half the total calculation time. The pressure values obtained by LBM are compared to the RANS solutions in Fig. 14 right, for the fan and fan-OGV stage, respectively. The small deviations observed can be attributed to the athermal and low-compressible approximations in *ProLB*.

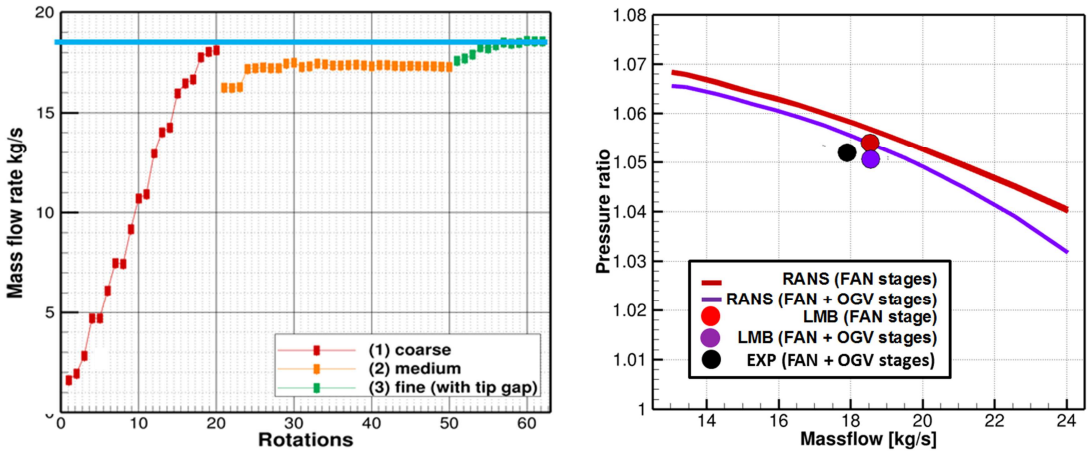

Fig. 14 Mass flow rate convergence from coarse to fine mesh set-up (left). Pressure ratio versus mass flow rate (right) provided by the LBM (at the end of the calculation) compared to RANS solutions at 45 Nn for various winnowing.

Nevertheless, a very good agreement between LBM and RANS is achieved in terms of mean velocity profiles as shown in Fig. 15, related to the axial velocity component extracted along a plane between the fan and OGV (x = 100 mm). The same trends between RANS and LBM methods are also observed on the static pressure in Fig. 15, right.

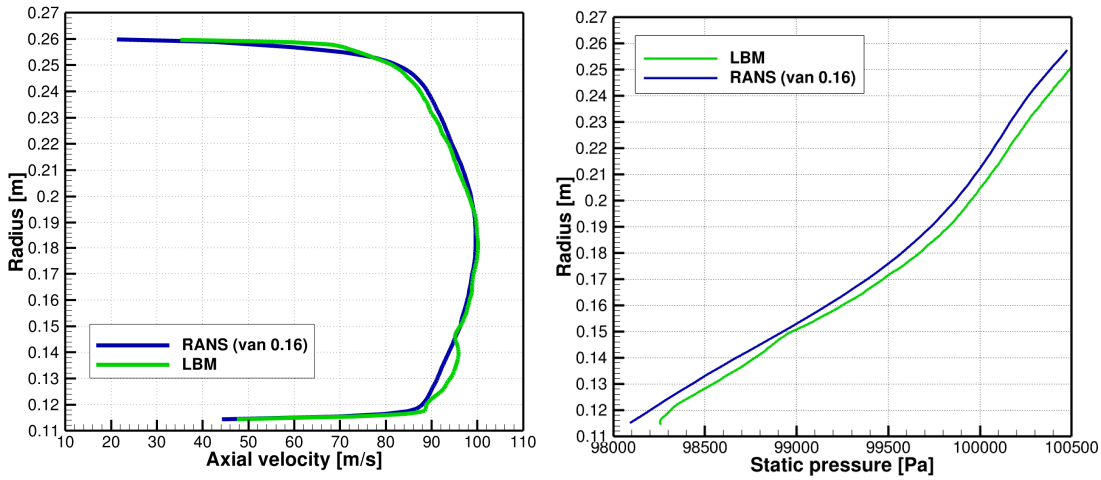

Fig. 15 Radial profiles of mean axial velocity (left) and static pressure (right) at x = 100 mm issued from RANS and LBM.

In addition to azimuthally averaged data in the inter-stage at x=100 mm, mean axial flow velocity (Fig. 16, left) and static pressure (Fig. 16, right) are plotted at x=250 mm downstream of the OGV stage. Behind the stator, the mesh has been coarsened both in LBM and RANS, which explains why wakes and boundary layers are more or less pronounced in the cross-sections of the solution field, even if the levels and trends are similar in both cases.

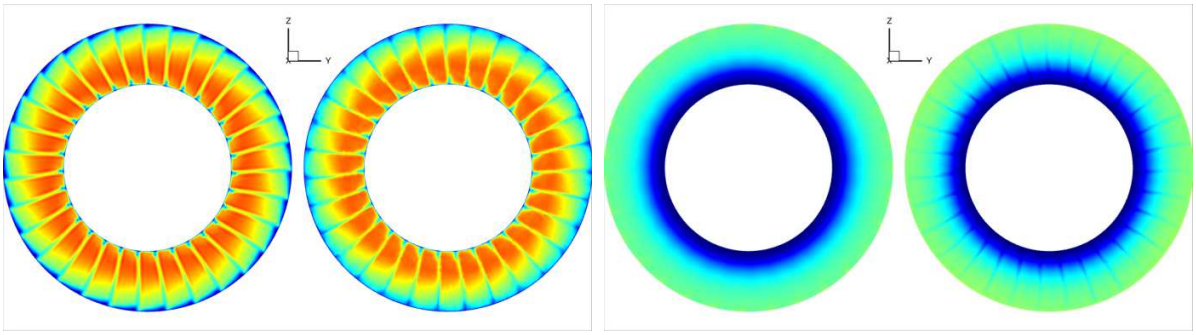

Fig. 16 Cuts at x=250 mm from RANS (left side of each subfigure) and LBM (right side of each subfigure). Axial velocity from 50 to 150 m/s (left) and static pressure from 98 to 101 kPa (right).

In order to compare the forces exerted on the solid surfaces, the wall pressure coefficient Cp is evaluated both on the reference rotor blade and stator vane at various radial positions according to:

$$\mathrm{Cp} = \frac{p - p_{ref}}{\frac{1}{2}\rho_{ref} U_{ref}^2}$$

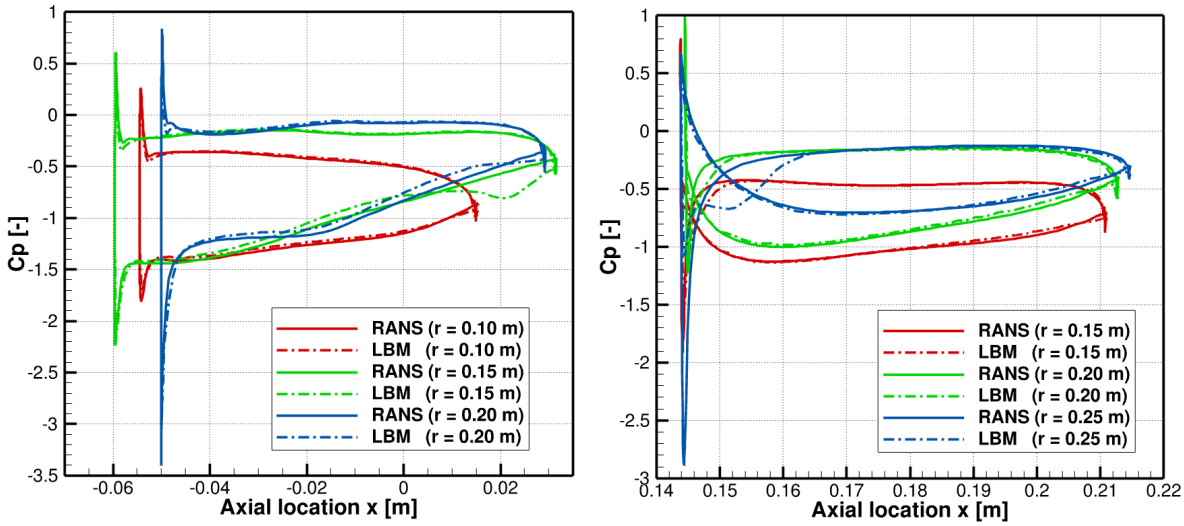

Fig. 17 Cp profile comparison at various radial positions for the rotor (left) and the stator (right).

In Fig. 17, a very nice agreement is observed between the RANS and LBM approaches, despite quite different set-up have been used (open configuration for LBM and closed one for RANS). However, there are two points of divergence, a local flow detachment at the trailing edge of the rotor (r = 0.15 m) and at the stator leading edge (r = 0.25 m). Regarding the first observation, it might also explain why turbulent wakes are supposedly too intense as discussed in the following aeroacoustics analyses. A decrease of this kind of flow detachment has been observed in previous studies [8] (in comparison with [35]) when refining the mesh. As concerns the second observations, it can be related to the tip flow modeling which is quite challenging to capture with a few points meshing this region and by relying on wall laws.

After assessing the stationary behavior of the flow, it is important to study its unsteady characteristics, which are the key mechanisms behind the broadband noise sources. Furthermore, the main focus of the unsteady aerodynamic analysis is on the turbulence wakes characteristics, because they are the main mechanism driving the rotor-stator interaction noise as discussed in parts dedicated to acoustics. Analysis of turbulent properties presented below relies on 16 rows of radially aligned probes placed 20% of stator vane chord upstream from their leading edges and depicted in Fig. 18 (left).

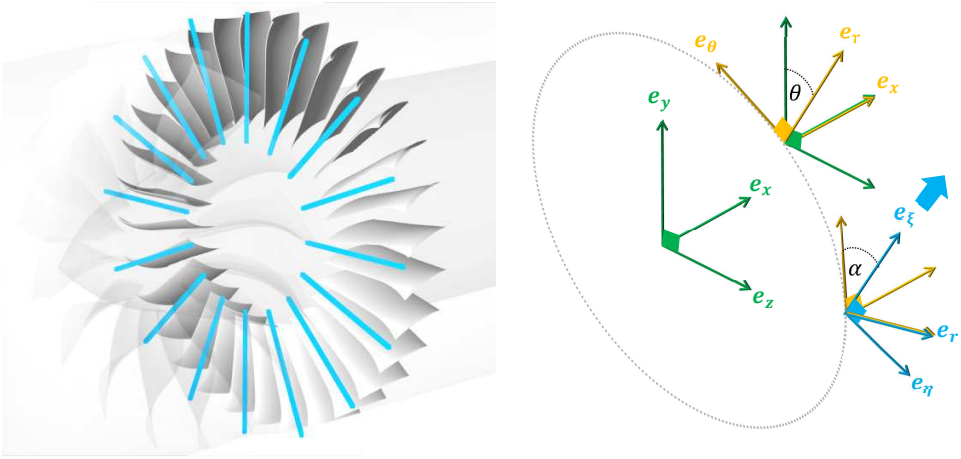

Fig. 18 Visualization of the probes rows used for post-processing of the unsteady data in the fan-OGV interstage (left). Diagram illustrating the changes of reference frame considered for the post-processing of wake turbulence (right).

In order to refocus the turbulent flow analysis along its preferred direction (while dissociating the radial component), a change of reference frame is implemented as follows:

$$\boldsymbol{u} = \begin{pmatrix} u_x \\ u_y \\ u_z \end{pmatrix}_{\boldsymbol{e_x},\boldsymbol{e_y},\boldsymbol{e_z}} \rightarrow \boldsymbol{v} = \begin{pmatrix} v_x \\ v_\theta \\ v_r \end{pmatrix}_{\boldsymbol{e_x},\boldsymbol{e_\theta},\boldsymbol{e_r}} \rightarrow \boldsymbol{w} = \begin{pmatrix} w_\xi \\ w_\eta \\ w_r \end{pmatrix}_{\boldsymbol{e_\xi},\boldsymbol{e_\eta},\boldsymbol{e_r}}$$

The three reference frames are depicted in Fig. 18, right. Furthermore, in order to isolate the velocity stochastic fluctuations, the standard genuine decomposition for a fluctuating quantity $\boldsymbol{q}$ is considered (as done for example in [22]):

$$\boldsymbol{q}(\boldsymbol{x},t) = \boldsymbol{q_{cyclo}}(\boldsymbol{x},t) + \boldsymbol{q_{stoc}}(\boldsymbol{x},t)$$
$$\boldsymbol{q_{cyclo}}(\boldsymbol{x},t) = \frac{1}{N}\sum_{n=1}^{N} \boldsymbol{q}(\boldsymbol{x},t+nT)$$

In the above equations, T is the period of the signature (1-blade passing time), and N_k is the number of time blocks. The stochastic fluctuations (turbulent part), $q_{stoc}(x,t)$, are classically obtained by substracting the phase-averaged (cyclostationary) part, $q_{cyclo}(x,t)$, to the total fluctuating field, $q(x,t)$. Practically, the phase-averaged signature is duplicated N_k times before realizing the substraction. Moreover, to enhance the statistics which are rather under-resolved due to the limited simulation time and thus to decrease statistical errors, a spatial averaging over the B = 16 probes (see Fig. 18, left) is also performed. To clarify the notation, $\boldsymbol{q_{stoc}}$ will be confounded with $\boldsymbol{q'}$. In the following analysis, the focus is set on the two major quantities describing a turbulent flow field, namely mean square velocities and length scales. The RMS velocity is defined as follows (with $\langle\ \ \rangle$ the ensemble average).

$$w_{ii}{}^{rms} = \sqrt{\langle w_i'^2 \rangle}$$

As for the turbulence length scales, two approaches are considered. First, in the time domain (as done for example in [23]):

$$L^t_{ii,\xi} = W_\xi \int_{t_0}^{t_1} \frac{\langle w_i'(t) \cdot w_i'(t+dt) \rangle}{\langle w_{ii}'^2 \rangle} dt$$

In theory t_1, should tend towards ∞. But, in practice due to spurious numerical oscillations, the integral is stopped at the first zero crossing. Second, in the frequency domain, an asymptotic extrapolation is performed following equation (6.213) in [24]:

$$L^f_{ii,\xi} = \lim_{f\to 0}\left(W_\xi \frac{S_{w_i'w_i'}(f)}{4\cdot\langle {w_{ii}'}^2\rangle}\right) = \lim_{f\to 0}\left(W_\xi \frac{\left(\widetilde{w'}_\iota(f)\right)^2}{4\cdot\langle {w_{ii}'}^2\rangle}\right)$$

Where $\widetilde{w'}_\iota$ denotes the Fourier transform of w_i' and $S_{w_i'w_i'}$ its power spectral density. As for the steady analysis, a convergence study of longitudinal fluctuating velocity and length scale is carried out in Fig. 19 by considering the data on single full revolutions at different times in the calculation.

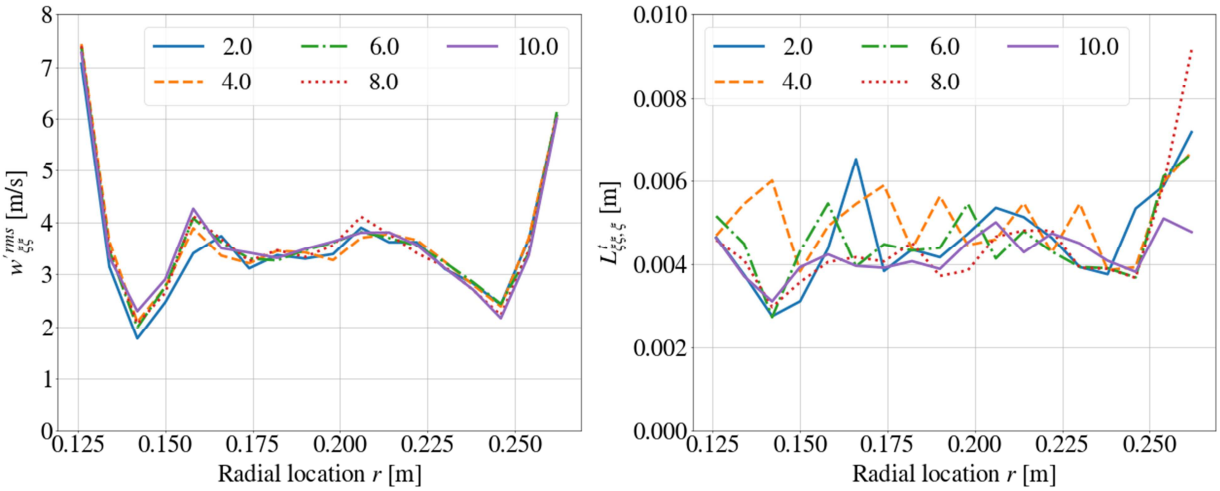

Fig. 19 Radial evolution of the RMS streamwise velocity post-processed from various single revolutions (left). Radial evolution of the streamwise length scale post-processed from various single revolutions (right).

While there seems to be little change in velocity fluctuations during the calculation, a higher variability is observed on the integral length scale. In fact, in the literature the characteristic length scales of the turbulence are in general much more challenging to accurately assess than for instance turbulence intensity both from RANS [1][25] and WLES simulation [8][23]. Nevertheless, as for the mean flow, the quantities appear to stabilize as early as the 6th revolution apart from the turbulence length scale at the shroud which exhibits a great discrepancy between successive revolutions. In any case, for the post-processing of turbulence that follows, 6 complete revolutions are considered (from the 6th to the 12th revolution). Furthermore, in Fig. 20, not only are the longitudinal properties of turbulence are considered, but also its transverse characteristics.

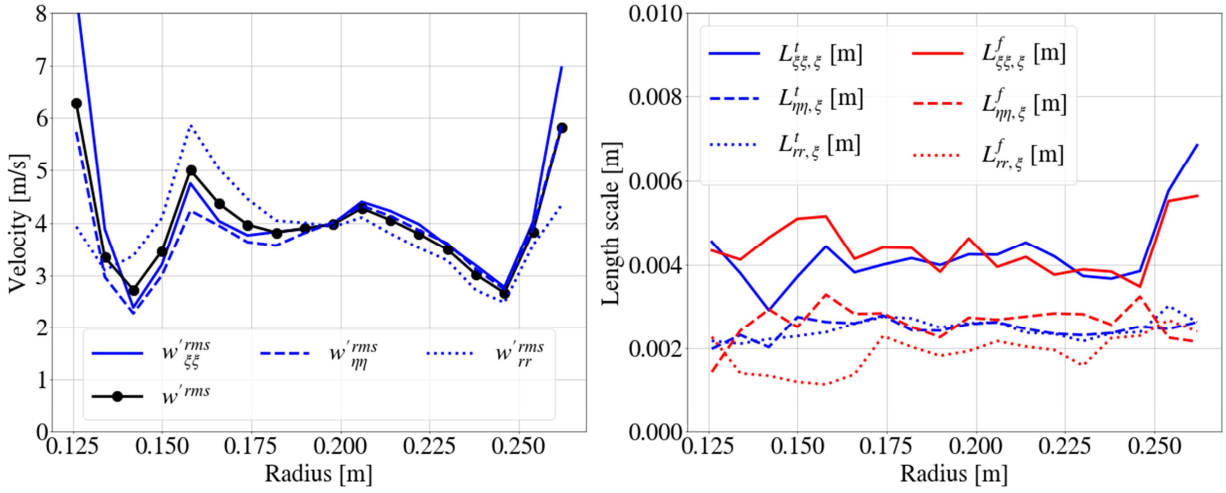

Fig. 20 Radial evolution of the RMS fluctuating velocities (left) and turbulent length scale (right). Post-processing performed over the 6 last revolutions.

First, it is interesting to study the curves in Fig. 20, left and right, with respect to the assumptions of a locally homogeneous and isotropic turbulence. First, it is found that close to the walls:

$$w_{ii}{}'^{rms} = \sqrt{\frac{1}{3}\left(\left(w_{\xi\xi}{}'^{rms}\right)^2 + \left(w_{\eta\eta}{}'^{rms}\right)^2 + \left(w_{rr}{}'^{rms}\right)^2\right)} \approx w_{\xi\xi}{}'^{rms} \approx w_{\eta\eta}{}'^{rms} \approx w_{rr}{}'^{rms},$$

which is consistent with [23]. However, the agreement is less satisfactory at the hub and shroud, which is consistent with the boundary layers locations. Moreover, especially near the hub, the strong geometric curvature of the duct makes the assimilation of the ξdirection with that of the flow less satisfactory. Second, as for the integral scale, it is found over a wide radial range that:

$$L_{\xi\xi,\xi} \approx 2 \cdot L_{\eta\eta,\xi} \approx 2 \cdot L_{rr,\xi}$$

which is in agreement with the isotropic turbulence theory. This observation has also been made in [23] on the NASA SDT benchmark test case, both from LBM post-processing and experimental data. Additionally, from a methodological standpoint, it is interesting to note that frequency-based and time-based approaches yield very similar trends. This result reinforces the relevance of the homogeneous and isotropic turbulence assumption in modeling the RSI noise. Nevertheless, it highlights that the stator upper and lower portions remain sensitive areas for acoustic noise prediction and reduction since stronger anisotropy appear near the boundary layers. In these areas, a more detailed study of all turbulence components concerning noise reduction, as done in [26], appears to be more comprehensive. Nevertheless, it is important to recall that an accurate modeling of wake turbulence remains challenging, especially regarding the convergence of results provided by RANS, WLES, or ZDES calculations with experimental data as discussed in [21][23][30].

As in [1][21][23][27][30], the data obtained here can feed available analytical models aiming to assess the RSI noise emitted by OGVs with/without LE serrations. For the serrated case, the Wiener-Hopf formulation previously discussed is adopted. For the baseline case (without serrations), the in-house code *TinA2D* [28] based on Amiet theory extended to ducted annular cascade is used for comparisons to the numerical predictions (see Sections V.A and V.B).

C. Direct acoustics and analogies-based predictions

Acoustic predictions have been recently obtained and only first relevant results are discussed here. The main objective of these LBM simulations is to assess if numerical simulation is able to provide the acoustic performances

of the low-noise serrated OGV (designed by ONERA) on a more complex configuration than previously implemented (a rectilinear cascade test-case in [8]). For this reason, the focus is put on the capture of OGV sources since the serrations are expected to reduce the leading edge noise from stator vanes generated by the RSI mechanism (resulting from interactions between the turbulent rotor blade wakes and the OGV). Furthermore, it should be emphasized that the RSI noise is expected to be the main source of broadband noise on this configuration as discussed in [21] (figure 4.23(b)) in comparison with the rotor alone emissions. This assertion will be discussed in the subsequent acoustic analyses. Nonetheless, the overall noise reduction achieved by serration should be caped by the rotor noise sources which are not tackled under this work.

The physical mechanisms at stake are qualitatively highlighted in Fig. 21, revealing the turbulent structures in the Fan-OGV interstage from the rotor and impacting the stator in term of iso-surfaces of Q-criterion (Fig. 21, left), the wall pressure distribution over the vanes (Fig. 21, right), and the acoustic waves radiated by the intake.

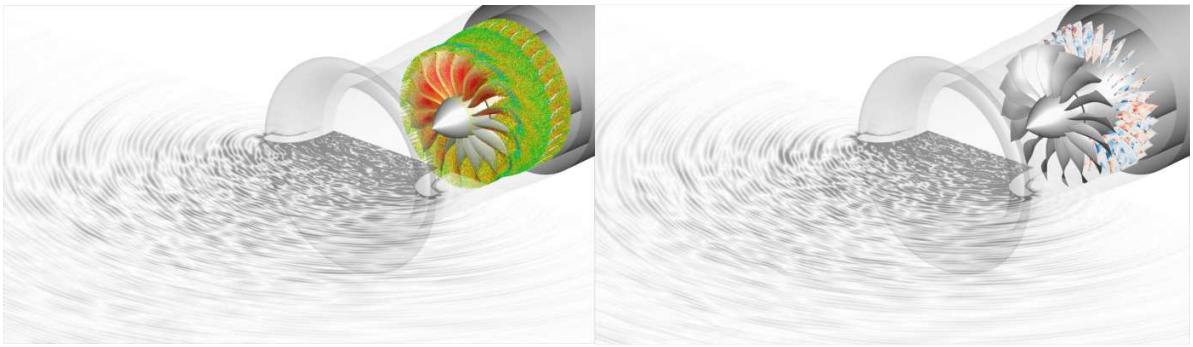

Fig. 21 Snapshot of LBM solution showing qualitative in-duct turbulent structures from iso Q-criterion surfaces colored by axial velocity (left), fluctuating wall pressure distributions over vanes (left), and radiated sound waves.

Acoustic analyzes are presented mostly in terms of sound power level spectra and by considering two main approaches: (1) the direct LBM solution providing the sound field radiated from the intake (acoustic field directly extracted on probes over spheres described in Fig. 13), and (2) the coupling with a FWH (solid surface) analogy restricted to the loading noise sources on the OGV. In this second approach, the in-duct propagation effects are included by adopting Goldstein's formulation [29], implemented in the in-house code *FanNoise* [30]. Practically, for spectrum analyzes, the temporal signal duration is covering at least 6 rotor revolutions, providing a frequency spacing of 16.5 Hz. In order to reduce inherent statistical errors, relevant PSD are currently assessed using the classical Welch method, but efficient sliding averaging functions (*Python* or *MATLAB* smoothing tools) are adopted here, more suitable for short duration signatures. Regarding the farfield acoustic analysis, a convergence assessment is first performed. To this end, we consider the averaged spectrum obtained at several microphones located at 2 meters from the intake. Results obtained for different starting full revolutions (from which the PSD is calculated) and limiting the signal duration to one revolution for this exercise, are depicted in Fig. 22 (left).

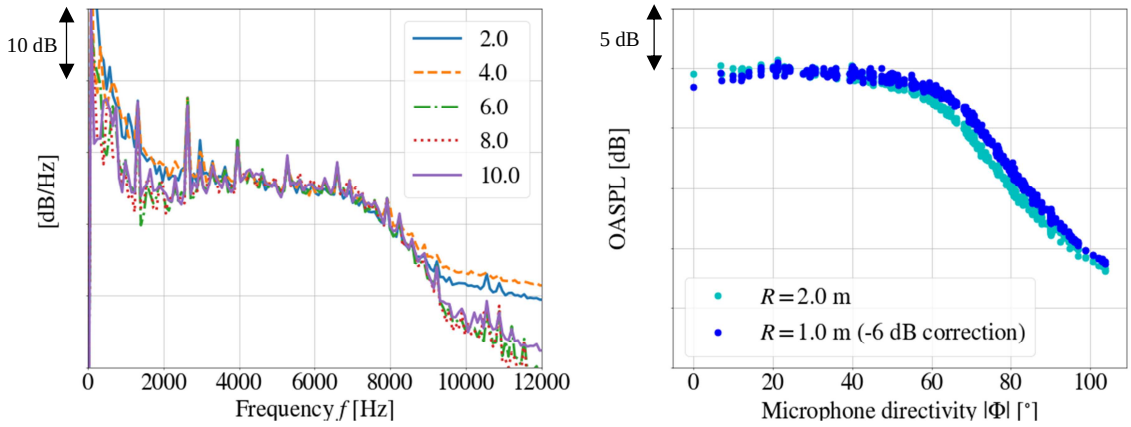

Fig. 22 Raw PWL spectra calculated from the signals over different single revolutions (left). OASPL levels (broadband part) at far-field intake microphones (levels integrated from 1 to 6 kHz).

The signals appear to converge starting from the 6th revolution (approximately halfway through the overall simulation time on a fine mesh) analogously to what has been observed for the mean flow or turbulent properties. For informational purposes, the temporal delay between the physical phenomena associated with turbulent wakes and the convection of acoustic waves to the far field microphones is approximately 70% of a single revolution time. For the subsequent acoustic analyses, the second half of the temporal signal obtained from the simulation can be considered. From a methodological perspective, revisiting the idea of using an acoustic zone at a distance of 1 meter for acoustic evaluations could be worthwhile. To this end, the OASPL levels (integrated between 1 and 6 kHz) for the different microphones of the two spheres are examined. By applying a -6dB correction (corresponding to doubling the distance for a perfectly spherical acoustic source), a very good agreement is observed between the two sets of microphones in Fig. 22 (right), in particular close to the x axis. Elsewhere, it can be legitimately thought that mesh dissipation at 2 m will be slightly greater when wave propagation is not aligned with the principal mesh directions.

PWL spectra related to each OGV (baseline and serrated) are compared in Fig. 23. In Fig. 23 left, both PWL spectra are related to the intake radiation from direct LBM solution (including all sources generated by rotor and stator), whereas in Fig. 23 right, the spectra are only related to the OGV sources propagating in the bypass duct (issued from *FanNoise*). In each case, a PWL reduction is clearly observed but it is more significant in Fig. 23 right, devoted to the OGV noise contribution.

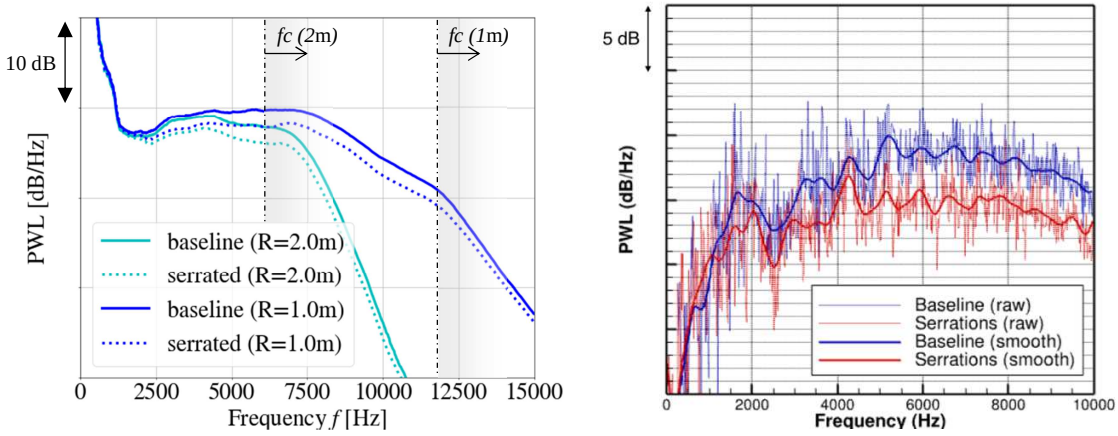

Fig. 23 PWL spectra for baseline and serrated cases assessed by LBM: radiated power from direct acoustic extractions at sphere locations (left) and bypass duct power from coupling with *FanNoise* (right).

In view of comparisons with measurements (Section V), specific analyzes have been performed with respect to the turbulent pressure on the vane surface obtained from LBM (*FanNoise* inputs), and to the behavior of FWH predictions when limiting the surface integration to the expected source region (RSI sources confined to LE region). RMS wall pressure fluctuations maps are plotted in Fig. 24, on vane suction side (picked at a frequency close to BPF2) for baseline and serrated cases. Three main points can be noticed: (1) most intense sources are located in the vicinity of the LE, (2) a source level reduction is clearly observed along the valleys of the serration patterns with maximum levels concentrated at the roots (as pointed out by numerous studies from the literature), (3) several zones with significant levels are present on the rest of the surface particularly for the serrated (secondary sources in the TE region). As investigated by Lewis [27], Polacsek [30], and Buszyk [8] the origin of such "extra sources" might be attributed to local flow detachments and/or vortical structures, captured here by LBM here (more analyzes to be done to status about reliable physics), which can pollute the radiated sound field involving the theoretical RSI mechanism. Additional calculations have been launched by considering limited surface integrations (depicted in Fig. 25, left) and resulting in PSD at bypass shroud (fully annular duct assumption in *FanNoise*), shown in Fig. 25 (right). A strong attenuation of the PSD level is observed, more significant at medium and high frequencies, and much more evidenced with the 30% chord integration. One should take advantage of this result in Section V, when comparing LBM+FWH predictions with solutions from semi-analytical models (derived from Amiet and Wiener-Hopf) and with experiments.

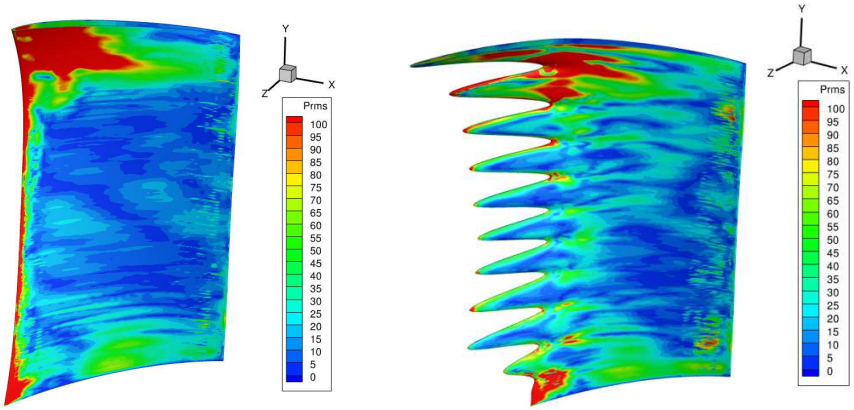

Fig. 24 RMS wall pressure on stator vane suction side: baseline (left) and serrated (right) case.

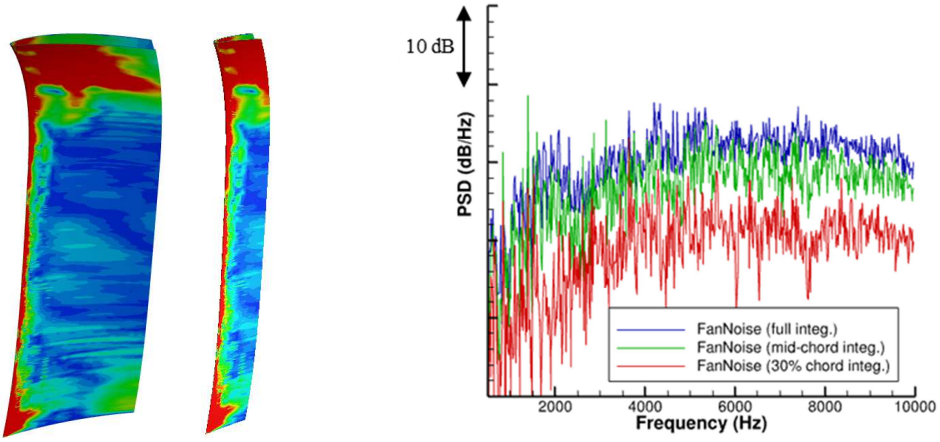

Fig. 25 On the left, chordwise limitation of FWH surface integation: 50% (left) and 30% (right) from LE. On the right, PSD at shroud from FanNoise predictions (baseline) for selected integration.

V. Comparisons with PHARE-B3 measurements

A. Aeroacoustic comparisons on the baseline case

The SPL spectra (from intake) at microphone 7 (see Fig. 2) assessed by LBM for baseline OGV is compared to the PHARE-B3 measurements in Fig. 26, left. The PSD shape is in good agreement with the experiment up to the maximum frequency reachable by the LBM mesh at the antenna position (or equivalent angular position at half the radius), but the predicted level is about 6 dB above the measurements. Further investigations are underway to understand this mismatch, mainly focusing on the mesh resolution at the rotor skin, which has not been refined further due to limited computational resources. Focusing on RSI sources on the OGV, PSD at bypass shroud assessed by *FanNoise* using the 3 integration surfaces previously discussed (same predictions than in Fig. 25 (right), but applying a sliding averaging leading to the present smoothed spectra) are compared to measurements at Mic.130 (one microphone of the linear array shown in Fig. 2, bottom). As discussed in [20], microphones at casing wall are located within the boundary layer and certainly polluted by the hydrodynamic modes tending to increase the low-frequency part of the spectrum when no filtering is applied (which is the case here). Regards to the exhaust comparison (Fig. 26, right), an overestimation of the levels is expected (since the LBM data are used as inputs), but the FWH predictions using full surface integration (blue curve) seems not reliable (more than 10 dB deviation), as the 30% chord integration result giving rise to an over-reduction of the level (since too much sources are truncated). The PSD obtained using a mid-chord integration is a good compromise choice (as discussed further below) and will be adopted for the following comparisons.

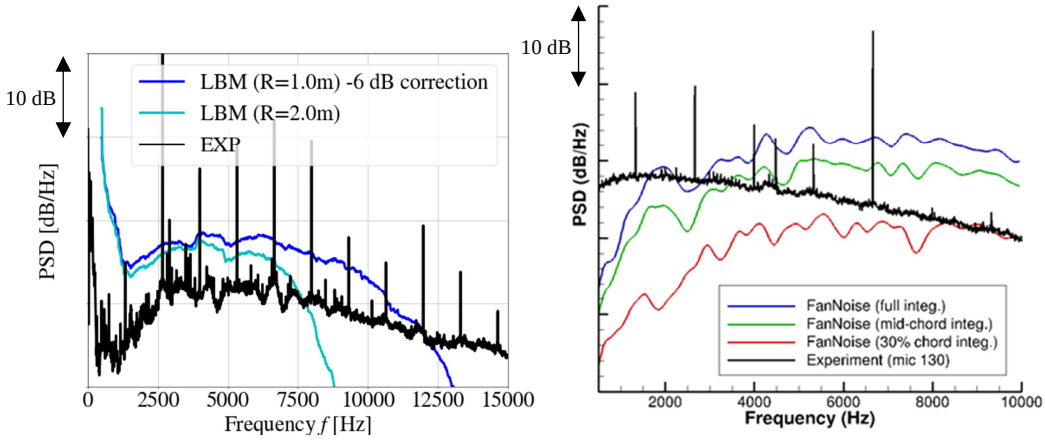

Fig. 26 SPL spectra of radiated sound field by intake at Mic. 7 (see Fig. 2) issued from direct LBM and measurements (left) and SPL spectra at bypass shroud issued from FanNoise and compared to measurements at Mic. 130 (right).

To take the comparison a step further between simulation and experimental data, two other approaches are assessed. First, the FWH-solid analogy is performed to evaluate the acoustic power both in the intake and in the bypass duct. Second, based on the turbulence properties discussed in Section IV.B, the Amiet-based solution (*TinA2D* code) is addressed too. In Fig. 27, an excellent agreement can be observed between *TinA2D* and *FanNoise* (using mid-chord integration) solutions, both in the intake (Fig. 27, left) and in the bypass (Fig. 27, right), and the predicted power spectra in the bypass are not far from the experiment issued from the ARMD [20][31] post-processing (Fig. 27, right). As discussed in [20], the ARMD technique proposed by Pereira [31] should be able to provide a good prediction of the acoustic power spectrum in the bypass duct, from array-processed sound field decomposition into modal and radial Fourier-Bessel modes, and then to obtain a representative estimator of the power reduction from serrated OGVs. However, the complete array measurements required for applying this technique were only acquired at selected regimes (55 Nn, 80 Nn and 90 Nn) and so the ARMD result at 45 Nn has been derived here from the measurements at 55 Nn and by applying a basic correction (spectrum ratio calibration from Amiet-based sound power predictions respectively at 55 Nn and 45 Nn regimes). Moreover, the indirect approaches are able to reproduce fairly well the direct LBM solution related to intake radiation (Fig. 27, left). Two hypotheses can be drawn. Firstly, it seems to confirm that the RSI mechanism is indeed the dominant source at play. Secondly, over-predicted levels observed in Fig. 27 (left), compared to measurements from external antenna, might be attributed to over-energized turbulence from rotor blades captured by LBM at this regime. To conclude on explanations, a more accurate study dedicated to mesh refinement sensitivity should be performed, and fan sources contribution should be evaluated too.

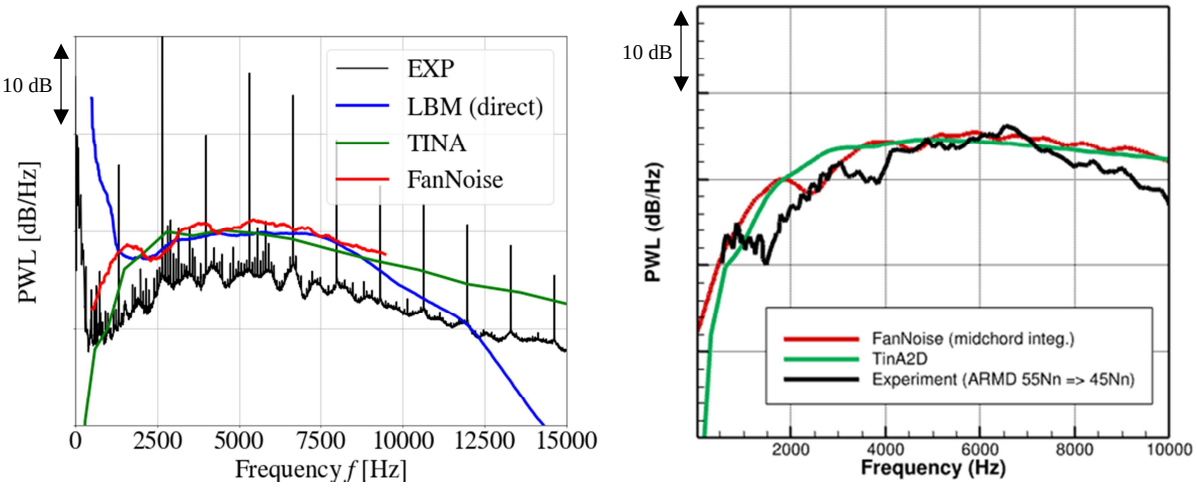

Fig. 27 All predictions vs. measurements: (left) PWL spectra radiated by intake issued from direct LBM, *FanNoise, TinA2D* and (right) PWL spectra in the bypass duct issued from *FanNoise, TinA2D* and ARMD.

B. Acoustic performances

Despite of the deviations previously observed on the absolute levels, a correct shape is found (similar trends are obtained on the serrated case not presented for conciseness), so that a relative PWL estimation between baseline and low-noise cases (ΔPWL spectrum assessment) should be reliable. The ΔPWL spectra resulting from the PWL assessments on baseline and serration cases are plotted in Fig. 28 and Fig. 29. The lower acoustic performances obtained on the upstream radiated field (Fig. 28) compared to the bypass (Fig. 29) can be due to the the rotor noise that could be more significant at this very low regime, partly masking the OGV contribution. Indeed, it was found from steady RANS calculations performed at 45 Nn (as discussed further below), that high flow detachments were present on blades and vanes, since the beta angles (designed for best aerodynamic performances at ADP) are badly aligned to the streamlines. As a consequence, additional sources might be created on the blade and vane walls that could also explain the lower PWL reductions obtained (even when focusing on OGV sources) compared to those issued from low-fidelity WH predictions in Fig. 29 (with PWL reductions up to 6 dB and ΔOAPWL around 4 dB). Nevertheless, ΔPWL levels from measurements are found higher than the predicted ones, reaching 3 dB upstream (Fig. 28) and 6 dB in the bypass duct using the ARMD estimations (Fig. 29) which is a very encouraging result. It should be noted that in high frequencies (above 7 kHz), the ARMD method is expected to overpredict the noise reduction, since the low-noise concept tends to decorrelate the noise sources and thus require a higher number of fixed reference sensors to carry out the analysis [20]. Hence, it can be outlined that this acoustic performance is close to WH-based prediction and also to the FWH-based prediction if the source integration is confined to the LE region (30% chord here). This suggests that these two practical methodologies (using present LBM input data) are quite relevant in order to assess the actual sound power reduction, assuming that the experimental PWL spectra derived by the ARMD estimator obtained at 55 Nn are trustful at 45 Nn.

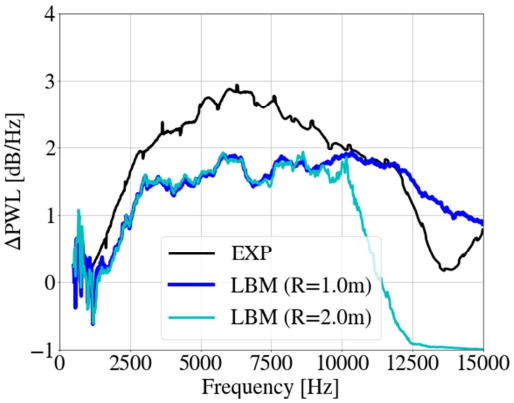

Fig. 28 ΔPWL spectra from intake radiation assessed by direct LBM and measurements.

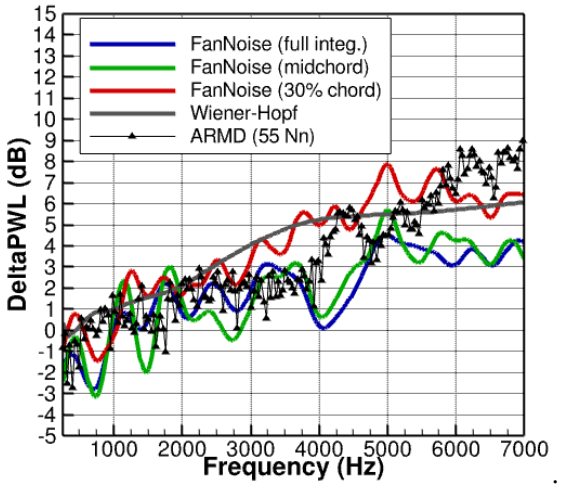

Fig. 29 ΔPWL spectra in the bypass duct assessed by *FanNoise* (full/mid/30% chord integration), WH, and compared to experiment (ARMD post-treatment).

It should be reminded that LBM simulations have been limited to the off-chart 45 Nn regime due to limitation in reachable Mach number (weakly compressible version of *ProLB* has been used under this project). Therefore, increasing the fan rotating speed is expected to have a beneficial impact on the achieved noise reduction and aerodynamic losses. The main reason for this is that, as the angular pitch is fixed, the offset between the local chord at the leading edge of the stator vanes and rotor blades relative to the incident flow will be minimized. In fact, the design of the test bed has been thought out with a view to obtain the best propulsive efficiency at nominal speed (100 Nn), as depicted in Fig. 30. For a better understanding of the RPM effect, mean flows from RANS computations at two regimes are compared in Fig. 30 (along with mean flow from LBM but only at 45 Nn).

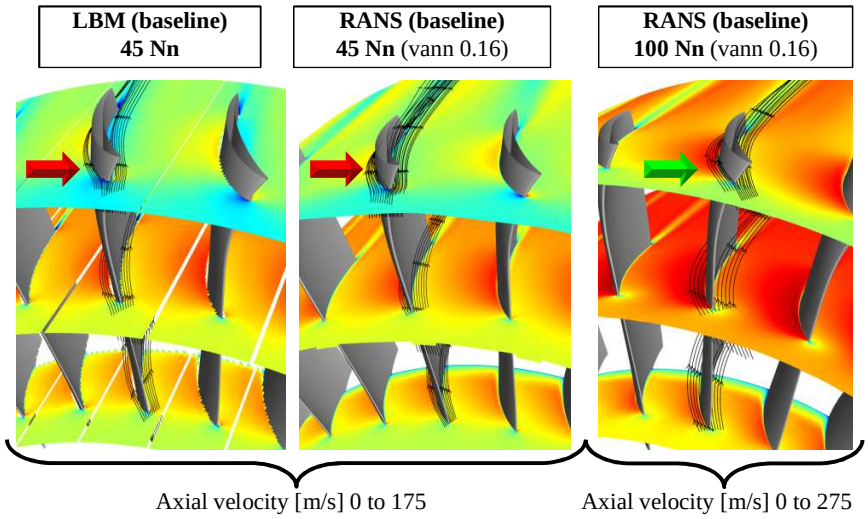

Fig. 30 Radial sections showing the axial mean flow and streamlines.

As illustrated in Fig. 30, mean flow streamlines are misaligned with the vanes leading edge at 45 Nn especially at the shroud (red arrows on Fig. 30). Indeed, the ECL5 turbofan model is at this RPM regime far from its nominal operating corresponding to 100 Nn. A very good alignment of the streamlines is found when obtained from 100 Nn, with a significant modification of the inflow angle at the shroud (green arrow). This angular offset at the low rotating speed may explain the significant pressure source observed at the casing in Fig. 24. It should be reminded that analytical model in Fig. 29 assumes a flat plate perfectly aligned with the incident mean flow. However, it is not easy to separate the influence of the improved flow alignment on noise reduction from other physical mechanisms at play at different engine regimes. However, quite significant sound power level reductions at higher RPM have also been assessed experimentally in [20], with broadband noise reduction illustrated in Fig. 31.

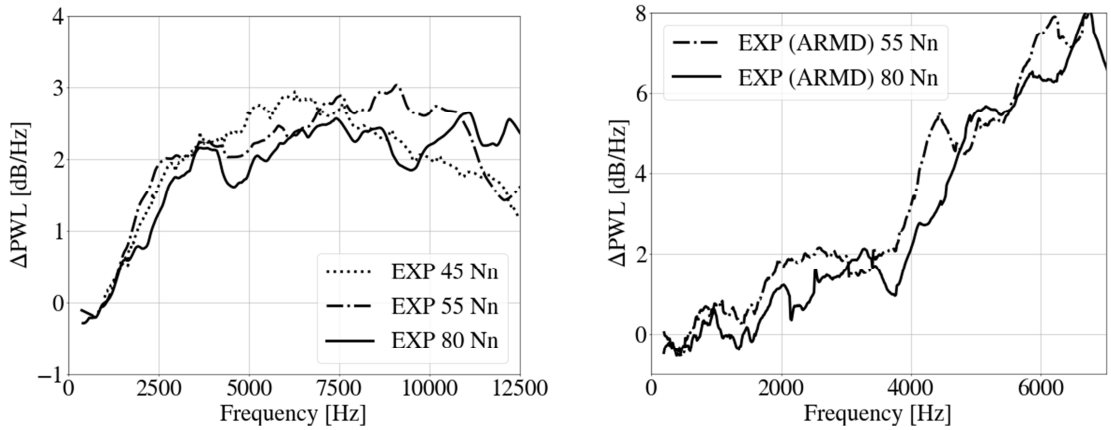

Fig. 31 PWL reduction (broadband part) from experimental data at other operating points from [20].

As expected from the literature [1][6][7][8][9], a shift towards higher frequency is expected when increasing the mean flow velocity (streamwise component roughly aligned with the OGV at LE position). This trend can be seen experimentally on the 45 Nn, 55 Nn, and 80 Nn regimes in Fig. 31 (broadband noise reduction only). In addition, as discussed in more detail in [20], aerodynamic losses are decreased when the rotational speed is increased which reinforces the analysis made from Fig. 30.

VI. Conclusion

This paper has clearly described the design stage with prediction methods dedicated to passive treatment for RSI noise reduction using sinusoidal leading edge serrations, which have been finally assessed during an experimental test campaign at ECL. In the present work, the attention was focused on broadband noise for which up to 3 dB PWL reduction has been achieved at the intake and 5 dB PWL in the bypass. Several prediction methods were used both during the design and evaluation phases. Firstly, based on semi-empirical models, a 2D pattern of wavy leading edge was proposed supplemented by analytical predictions based on a Wiener-Hopf formulation. An in-house modeler (*ersatZ*) was then used to design and provide 3D geometries derived from the initial 2D pattern. An iterative process allowed, after several iterations based on RANS simulations, to select a final geometry, with aerodynamic penalties reaching the target values prescribed by SAE, and which has been manufactured by COMOTI. Before the experimental test campaign, an LBM simulation was also set up, for a low-speed regime suitable to the code ability, to estimate the noise reduction achievable with the proposed concept. From this simulation, several methodologies for predicting noise and its reduction could be compared: either by direct calculation at microphones location or by considering indirect approaches. For the latter, an analytical solution based on Amiet's theory fed with post-processed turbulence data from the LBM calculation has been addressed, in addition to a FWH solver assessing the loading noise generated by the stator vanes (accounting for in-duct propagation following Goldstein's approach). These different approaches have shown a very good agreement between them, confirming the idea that the RSI mechanism is the main component of the broadband noise observed on this turbofan model. A good agreement in terms of noise spectra shapes was also observed with experimental data, despite an over prediction of the radiated noise. However, the agreement was even better when focusing on relative comparisons between the baseline and low-noise geometries, by focusing for example on ΔPWL spectra achieved at intake and bypass.
Future work should be devoted to a finer analysis of turbulent wake sensitivity, and thus RSI, to rotor mesh. For this purpose, rotor oriented simulations coupled with analytical solution (*Tina2D* for instance) to predict RSI appear quite relevant as pointed out in this work. In addition, fan alone noise contribution could be assessed by *FanNoise* using LBM-based turbulent pressure field on the rotor blades. Regarding the OGV stage, a finer refinement at the skin should also reduce the contribution of the extra sources which are expected to partially pollute the LE noise source in high frequencies as pointed out in [8][35]. CPU cost of these additional studies is nevertheless non-negligible. Finally, noise reduction treatments are of particular interest for engine manufacturers as SAE for their future architectures. Furthermore, particular attention should be paid to optimization techniques of these treatments for which the adjoint method appears especially suitable [36][37].

Acknowledgments

The authors would like to greatly thank COMOTI for their support in the ONERA's CAD file generation and manufacturing of serrated OGV (31 vanes). This study has received respective funding from the Clean Sky 2 Joint Undertaking (JU) under the European Union's Horizon 2020 research and innovation program under grant agreement n°865007 (InnoSTAT project), and from European Union's Horizon 2020 research and innovation program in the frame of ADEC project of CS2 LPA-IADP.

References

[1] Polacsek, C., Cader, A., Buszyk, M., Barrier, R., Gea-Aguilera, F., and Posson, H., *Aeroacoustic Design and Broadband Noise Predictions of a Fan Stage with Serrated Outlet Guide Vanes*, Physics of fluids, Vol. 32, No. 10, 2020. https://doi.org/10.1063/5.0020190

[2] Schneider, A. P., Fiquet, A., Paoletti, B., Ottavy, X., and Brandstetter, C. (March 11, 2024). "*Experiments on Tuned UHBR Open-Test-Case Fan ECL5/CATANA: Performance and Aerodynamics*." ASME. J. Turbomach. August 2024; 146(8): 081001. https://doi.org/10.1115/1.4064231

[3] Brandstetter, C., Fiquet, A., Schneider, A. P., Paoletti, B., and Ottavy, X. (December 11, 2023). "Experiments on Tuned UHBR Open-Test-Case Fan ECL5/CATANA: Stability Limit." ASME. J. Eng. Gas Turbines Power. May 2024; 146(5): 051011. https://doi.org/10.1115/1.4063717

[4] Brandstetter, Christoph & Pagès, Valdo & Duquesne, Pierre & Ottavy, Xavier & Ferrand, P. & Aubert, Stéphane. (2021). UHBR open-test-case fan ECL5/CATANA part 1: geometry and aerodynamic performance. 10.29008/ETC2021-626. https://doi.org/10.29008/ETC2021-626

[5] Pagès, V.; Duquesne, P.; Aubert, S.; Blanc, L.; Ferrand, P.; Ottavy, X.; Brandstetter, C. UHBR Open-Test-Case Fan ECL5/CATANA. Int. J. Turbomach. Propuls. Power 2022, 7, 17. https://doi.org/10.3390/ijtpp7020017

[6] Paruchuri, C., Joseph, P., Narayanan, S., Vanderwel, C., Turner, J., Kim, J. W., and Ganapathisubramani, B., *Performance and mechanism of sinusoidal leading edge serrations for the reduction of turbulence–aerofoil interaction noise*, Journal of Fluid Mechanics, Vol. 818, 2017. doi:10.1017/jfm.2017.141

[7] M. Buszyk, C. Polacsek, T. Le Garrec, R. Barrier and C. Bailly, *Numerical Assessment of Turbulence-Cascade Noise Reduction and Aerodynamic Penalties from Serrations*, AIAA Journal, Vol. 60 (6), June 2022. https://doi.org/10.2514/1.J061301

[8] M. Buszyk, C. Polacsek, T. Le Garrec, R. Barrier, V. Clair, E. Salze, and C. Bailly, *Aeroacoustic Assessment of a Rectilinear Cascade with Leading Edge Serrations: Predictions and Measurements*, Computers & Fluids, Vol. 271, March 2024. https://doi.org/10.1016/j.compfluid.2024.106179

[9] L. Ayton and C. Paruchuri, *An analytical and experimental investigation of aerofoil–turbulence interaction noise for plates with spanwise-varying leading edges*, Journal of Fluid Mechanics, 865:137–168, 2019. doi: 10.1017/jfm.2019.78.

[10] D. Casalino, F. Avallone, I. Gonzalez-Martino, and D. Ragni. *Aeroacoustic study of a wavy stator leading edge in a realistic fan/OGV stage*, Journal of Sound and Vibration, 442:138–154, 2019. ISSN 0022-460X. doi: https://doi.org/10.1016/j.jsv.2018.10.057.

[11] M. Daroukh, T. Le Garrec, and C. Polacsek, *Low-speed turbofan aerodynamic and acoustic prediction with an isothermal lattice Boltzmann method*, AIAA Journal, 60(2):1152–1170, 2022. doi: 10.2514/1.J060752. URL https://doi.org/10.2514/1.J060752.

[12] 2022. URL http://www.prolb-cfd.com/

[13] Shan, X.-F. Yuan, and H. Chen. Kinetic theory representation of hydrodynamics: a way beyond the Navier–Stokes equation. Journal of Fluid Mechanics, 550:413–441, 2006. doi: 10.1017/S0022112005008153.

[14] N. Afzal. Wake layer in a thermal turbulent boundary layer with pressure gradient. International Journal of Heat and Mass Transfer, 1999. 10, 39, 88, 147, 165.

[15] S. Wilhelm, J. Jacob, and P. Sagaut. An explicit power-law-based wall model for lattice Boltzmann method-Reynolds-averaged numerical simulations of the flow around airfoils. Physics of Fluids, 30, 2018. 9, 10, 11, 39, 147. https://doi.org/10.1063/1.5031764

[16] J. Jacob, O. Malaspinas, and P. Sagaut. A new hybrid recursive regularised Bhatnagar–Gross–Krook collision model for lattice Boltzmann method-based large eddy simulation. Journal of Turbulence, pages 1 – 26, Nov. 2018. doi: 10.1080/14685248.2018.1540879. URL https://hal.archives-ouvertes.fr/hal-02114308.

[17] S. Guo, Y. Feng, J. Jacob, F. Renard, and P. Sagaut. An efficient lattice Boltzmann method for compressible aerodynamics on d3q19 lattice. Journal of Computational Physics, 418:109570, 2020. ISSN0021-9991. doi: https://doi.org/10.1016/j.jcp.2020.109570.

[18] E. Lévêque, F. Toschi, L. Shao, and J.-P. Bertoglio. Shear-improved Smagorinsky model for large-eddy simulation of wall-bounded turbulent flows. Journal of Fluid Mechanics, 570:491–502, 2007. doi: 10.1017/S0022112006003429.

[19] T. Astoul, G. Wissocq, J.-F. Boussuge, A. Sengissen, and P. Sagaut. Lattice Boltzmann method for computational aeroacoustics on non-uniform meshes: A direct grid coupling approach. Journal of Computational Physics, 447:110667, Dec. 2021. doi: 10.1016/j.jcp.2021.110667.

[20] Salze, E., Pereira, A., Brandstetter, C., and Clair, V. “Noise reduction of aero-engines using innovative stators with leading edge features”, to be presented at the 30th AIAA/CEAS in June 2024.

[21] Al Am, J., Clair, V., Giauque, A., Boudet, J., "Direct noise predictions of a fan brodband noise using LES an analytical models", AIAA, 2022. https://doi.org/10.2514/6.2022-2882

[22] François, B., Barrier, R., and Polacsek, C.,“Zonal Detached Eddy Simulation of the Fan-OGV Stage of a Turbofan Engine: PartI—Methodology, Numerical Setup and Aerodynamic Analysis,” ASME J. Turbomach., 2022. https://doi.org/10.1115/1.4054528

[23] S. Grace, I. Gonzalez-Martino, and D. Casalino. Analysis of fan-stage gap-flow data to inform simulation of fan broadband noise. Philosophical Transactions of the Royal Society A: Mathematical, Physical and Engineering Sciences. doi: 10.1098/rsta.2019.0080.

[24] S. B. Pope. Turbulent Flows. Cambridge University Press, 2000. doi: 10.1017/CBO9780511840531.

[25] C. Kissner, S. Guérin, P. Seeler, M. Billson, P. Chaitanya, P. Carrasco Laraña, H. de Laborderie, B. François, K. Lefarth, D. Lewis, G. Montero Villar, and T. Nodé-Langlois. ACAT1 benchmark of rans-informed analytical methods for fan broadband noise prediction—part i—influence of the rans simulation. Acoustics, 2(3):539–578, 2020. ISSN 2624-599X. https://doi.org/10.3390/acoustics2030029

[26] F. G. Aguilera, J. R. Gill, D. Angland, and X. Zhang. Wavy Leading Edge Airfoils Interacting with Anisotropic Turbulence. 2017. doi: 10.2514/6.2017-3370. URL https://arc.aiaa.org/doi/abs/10.2514/6.2017-3370.

[27] Lewis, D., Moreau, S., Jacob, M. C., and Sanjosé, M., 2021, “ACAT1 Fan Stage Broadband Noise Prediction Using Large-Eddy Simulation and Analytical Models,” AIAA J., 60(1), pp. 360–380. https://arc.aiaa.org/doi/abs/10.2514/1.J060163
[28] Reboul, G., Polacsek, C., Lewy, S., and Heib, S., 2008, “Ducted-Fan Broadband Noise Simulations Using Unsteady or Averaged Data,” INTER-NOISE and NOISE-CON Congress and Conference Proceedings, Shanghai, China, Oct. 26–29, pp. 1454–1469, 2008.
[29] Goldstein, M.-E., "Aeroacoustics", McGraw-Hill, New York, pp. 63–66, 1976.
[30] Polacsek, C., Daroukh, M., François, B., and Barrier, R., “Zonal Detached Eddy Simulation of the Fan-OGV Stage of a Turbofan Engine: Part II— Broadband Noise Predictions”, ASME J. Turbomach., pp. 1–34, 2022. https://doi.org/10.1115/1.4054764
[31] Pereira, A., Jacob, M.C., "Modal analysis of in-duct fan broadband noise via an interative bayesian inverse approach", J. Sound Vib., Vol. 520, 2022. doi: 10.1016/j.jsv.2021.116633.
[32] Totu, A.-G.; Cican, G.; Crunțeanu, D.-E. Serrations as a Passive Solution for Turbomachinery Noise Reduction. Aerospace 2024, 11, 292. https://doi.org/10.3390/aerospace11040292
[33] F. Tong, W. Qiao, K. Xu, L. Wang, W. Chen, and X. Wang. On the study of wavy leading-edge vanes to achieve low fan interaction noise. Journal of Sound and Vibration, 419:200–226, 2018. ISSN 0022-460X. doi: https://doi.org/10.1016/j.jsv.2018.01.017.
[34] Teruna, Christopher & Rego, Leandro & Casalino, Damiano & Ragni, Daniele & Avallone, Francesco. (2022). A Numerical Study on Aircraft Noise Mitigation Using Porous Stator Concepts. Aerospace. 9. https://doi.org/10.3390/aerospace9020070
[35] M. Buszyk, T. Le Garrec, C. Polacsek, R. Barrier. Lattice Boltzmann simulations in a rectilinear cascade configuration for the turbulence-airfoil interaction noise evaluation and reduction through serrated leading edges. EURONOISE 2021, Oct 2021, online, Portugal. ⟨hal-03396128⟩
[36] Hajczak, A., Buszyk, M. “Shape optimization of 2D airfoils for propeller broadband noise mitigation using the adjoint method and semi-analytical models”, to be presented at the 30th AIAA/CEAS in June 2024.
[37] Foglia, E., Daroukh, M., Buszyk, M., Salah el-Din, I., Moreau, S. “Towards the optimization of propeller tonal noise in the frequency domain using the discrete adjoint method”, to be presented at the 30th AIAA/CEAS in June 2024.